Facile synthesis approach for core-shell TiO_2–CdS nanoparticles for enhanced photocatalytic H_2 generation from water

Muhammad Zubair,[a] *Ingeborg-Helene Svenum,*[a, b] *Magnus Rønning,*[a] *and Jia Yang* [a,*]

[a.] Department of Chemical Engineering, Norwegian University of Science and Technology (NTNU), Sem Sælands vei 4, NO-7491, Trondheim, Norway.

[b.] SINTEF Industry, P. O. Box 4760 Torgarden, N-7465, Trondheim, Norway

*** Corresponding Author: Tel: +4773593146**

E-mail address: [*] **jia.yang@ntnu.no**

ABSTRACT

With the ambition to design a cost-effective and highly stable photocatalyst with improved photocatalytic activity towards H_2 generation by water splitting, herein we report a two-step facile synthesis approach for core-shell structure of TiO_2-CdS nanocomposites. The synthesized photocatalysts are comprehensively characterized by SEM, XRD, BET, UV-vis DRS, Photoluminescence and XPS to investigate the morphological, crystalline, structural, optical properties and surface analysis. The photocatalytic activity is evaluated by measuring the ability of TiO_2-CdS to generate H_2 gas by water splitting in the presence of hole scavengers under simulated solar light at AM 1.5G conditions. Our optimized sample TiO_2-CdS (3:2) exhibited an enhanced photocatalytic activity by generating 954 μmol g^{-1} h^{-1} of hydrogen which is ~1.4 and ~1.7 times higher than pure CdS nanoparticles and pure TiO_2, respectively. The optimized sample achieved an apparent quantum efficiency of 3.53% along with good stability by generating a similar amount of H_2 for 40 consecutive hours. The enhanced photocatalytic activity and stability of the core-shell TiO_2-CdS nanocomposite is attributed to the broader solar spectrum absorption, efficient photo-induced charge separation on the interface of TiO_2-CdS due to the formation of heterojunction and high surface area with a large fraction of mesopores.

Keywords: Core-Shell TiO_2-CdS nanocomposite, Photocatalytic H_2 generation, CdS nanoparticles, hydrothermal approach, Heterojunction

1. Introduction

To overcome the environmental issues which are associated with the utilization of fossil fuels, hydrogen (H_2), a renewable, clean and zero-carbon emission energy carrier can be a promising alternative for sustainable development [1], which can be generated photocatalytically by utilizing semiconductors using the sunlight [2]. Among many different photocatalysts [3–10], cadmium sulfide (CdS) is a n-type photocatalyst, having a band gap of 2.4 eV with suitable band edge position relative to the redox potential of water, brilliant charge transport properties, and electronic mobility, and therefore is considered as an efficient and promising photocatalyst [11]. Despite its alluring properties, the issues related to rapid charge recombination and the photo-corrosion keep it far away from commercial application [12]. To overcome these bottlenecks, different strategies including CdS based solid solutions formations, co-catalysts loading, coupling with other semiconductors and carbon-based heterojunctions have been implemented [13]. Among all these strategies core-shell heterojunction formation of CdS with TiO_2 is considered an attractive approach due to the dual role played by the shell of TiO_2. The shell of TiO_2 covering CdS shields it from photo-corrosion and increases the charge separation efficiency by forming the in-built heterojunction, in turn achieving higher stability and activity.

The coupling of CdS with TiO_2 in the form of a core-shell structure may be the key to obtain higher activity and stability for photocatalytic H_2 generation due to efficient charge separation and broader light spectrum absorption. The shell of TiO_2 over CdS nanoparticles will make a type II heterojunction photocatalytic material leading to higher photocatalytic efficacy [14]. The core-shell nanocomposite of TiO_2 and CdS will also ensure cost-effective and efficient photocatalysts without using noble metals and complicated synthesis procedures. At present, many different TiO_2-CdS photocatalysts have been investigated for different photocatalytic applications including water splitting for H_2 generation [15–17]. Lee and Wang [18,19] investigated the effect of formation of a heterojunction between CdS and TiO_2 in photocatalytic

H_2 generation in the presence of hole scavengers and confirmed that the increase in the photocatalytic activity for H_2 generation is due to the formation of a heterojunction between CdS and TiO_2. Fang *et. al.* [20] have synthesized the core-shell structure of TiO_2-CdS with different thickness of TiO_2, and concluded that the enhanced photoelectrochemical properties is due to the formation of a heterojunction and fast electron transfer from CdS to TiO_2. The mesoporous core-shell CdS@TiO_2 1D and 2D photocatalysts synthesized by Nada *et. al.* [17] exhibited enhanced photocatalytic H_2 generation activity and stability with the deposition of Pt metal on nanocomposite in basic pH conditions. They attribute this to the morphological effect of CdS and the formation of the core-shell structure of TiO_2-CdS. However, very few reports on core-shell TiO_2-CdS structure for water splitting with facile synthesis methods are available and still there is a need to investigate the effect of TiO_2 over CdS to enhance the photocatalytic activity and stability for H_2 generation from water.

Herein, we present a study of core-shell nanocomposites of TiO_2–CdS photocatalysts with varying shell thickness, synthesized by a facile two-step hydrothermal method. In step I, CdS nanoparticles with a size of ~70 nm are synthesized by mixing cadmium acetate with thiourea in water using a hydrothermal method. In step II, a TiO_2 shell is synthesized over the CdS nanoparticles by adding titanium (IV) isopropoxide in ethanol solution containing highly dispersed CdS nanoparticles followed by hydrothermal treatment. The as-synthesized photocatalysts are comprehensively characterized by several characterization tool, and photocatalytic activity is evaluated for photocatalytic H_2 generation by water splitting under simulated solar light at AM 1.5G conditions.

2. Experimental Section

2.1. Materials and reagents

For the synthesis of pure CdS nanoparticles, pure TiO_2 and core-shell TiO_2-CdS nanocomposite samples, cadmium acetate dehydrated ($Cd(OOCCH_2)_2•2H_2O$, 98%) and titanium (IV) isopropoxide (TTIP, 98%) were purchased from Sigma-Aldrich. Thiourea ($SC(NH_2)_2$, ACS. ≥ 99%) and absolute ethanol (C_2H_5OH) were ordered from Alfa Aesar and VWR CHEMICALS, respectively. Sodium sulfite anhydrous (Na_2SO_3, 98%) and sodium sulfide nanohydrate ($Na_2S•9H_2O$, ACS. 98%) were purchased from Alfa Aesar and deionized (DI) water was used in the entire study.

2.2. Synthesis of pure CdS nanoparticles

Pure CdS nanoparticles were synthesized by following a previously reported method [21]. In brief, 0.9 g of cadmium acetate dehydrated and 2.63 g of thiourea were dissolved in 60 ml of DI water to make a clear solution to synthesize 200 mg of stoichiometric CdS nanoparticles. After stirring for 30 min, the resulting solution was transferred to a Teflon-lined hydrothermal autoclave having a volume of 90 ml. The firmly sealed hydrothermal autoclave was kept in the box furnace at 180 °C for 18 h, after which it was allowed to cool down naturally to room temperature. The orange colored CdS nanoparticles were removed from the hydrothermal autoclave and washed with DI water several times followed by drying at 80 °C for 12 h.

2.3. Synthesis of core-shell TiO_2-CdS nanocomposite

For the synthesis of core-shell TiO_2-CdS nanocomposite, 200 mg of as-synthesized CdS nanoparticles were properly dispersed in 40 ml of C_2H_5OH by stirring, followed by 30 min of ultrasonication to obtain a uniform mixture. Varying amounts of TTIP was then added to the uniform mixture under vigorous stirring followed by dropwise addition of 20 ml of DI water. After stirring for 1 h, the mixture was transferred to a Teflon-lined hydrothermal autoclave and

heated at 180 °C for 18 hr in a box furnace. After the hydrothermal reaction, the autoclave was allowed to cool down naturally to room temperature. The core-shell TiO_2-CdS nanocomposite was collected from the autoclave, and washed with DI water many times, and finally dried at 80 °C for 12 h. To investigate the role of shell thickness of TiO_2 at CdS for photocatalytic H_2 generation from water, different samples with varying weight ratio of TiO_2 to CdS were synthesized. For the synthesis of different TiO_2-CdS nanocomposite samples, stoichiometric x ml of TTIP (x= 0.18, 0.37, 0.55 and 0.74 ml) was added to 200 mg CdS nanoparticles dispersed in C_2H_5OH, to achieve the TiO_2-CdS (1:2), TiO_2-CdS (2:2), TiO_2-CdS (3:2) and TiO_2-CdS (4:2) samples respectively. For comparison, a pure TiO_2 sample was also synthesized following the same procedure without CdS nanoparticles.

2.4. Characterization techniques

The crystalline structure of all the samples was examined by powder X-ray diffraction (XRD) in the range $2\theta = 10\text{-}75°$ using an X-ray diffractometer (D8 A25 DaVinci, Bruker) with variable divergence slit using Cu Kα radiation ($\lambda = 1.54$ Å). The topological analysis of as-synthesized photocatalysts was done by using the in-lens cold field emission electron microscope FE-S(T)EM, (Hitachi S-5500) equipped with a dark field detector for transmission images. To measure the specific surface area of all the samples, N_2 sorption isotherms were obtained at -196 °C using a Micromeritics (TriStar II 3020) apparatus. The Brunaner-Emmett-Teller (BET) equation and Barret-Joyner-Halenda (BJH) equations are used to calculate the specific area from the N_2 sorption isotherms and average pore width by the desorption isotherms, respectively. To test the optical response of the prepared material, UV-vis diffuse reflectance spectra (DRS) were measured in the range of 200-900 nm by a fiber optic spectrometer (AvaSpec – 2048) coupled with an integrating sphere. Photo-luminescence (PL) spectra were

recorded using a Horiba Fluorology-3 fluorometer. For PL measurements, the solid samples were dispersed in water to make a suspension. Surface analysis and the valence states of the elements present in pure CdS, pure TiO_2, and TiO_2-CdS nanocomposite were performed by X-ray photoelectron spectroscopy (XPS) (Axis Ultra DLD XP spectrometer, Kratos Analytical) using monochromated Al Kα radiation (1486.6 eV). The core level spectra were measured using a pass energy of 20 eV, and all the peaks were calibrated against the C 1s component of adventitious carbon at 284.8 eV.

2.5 Photocatalytic H_2 generation tests

The tests for photocatalytic H_2 evolution from water splitting were carried out using a side-irradiated quartz photoreactor having a volume of 1.2 liters connected with an Ar gas flowing system as shown in Fig. S1. Typically, 40 mg of the as-synthesized photocatalytic material is appropriately dispersed in 600 ml aqueous solution of 0.125 M Na_2S and 0.175 M Na_2SO_3 acting as hole scavengers. The photoreactor containing the suspension was then sealed, and Ar gas was purged (100 mL min^{-1}) through the reactor for 30 min to remove the dissolved oxygen from the photoreactor in the dark. After degassing, the photoreactor with flowing Ar as a carrier gas was irradiated with simulated solar light using a 150 W Xenon solar simulator (SCIENCETECH SS150) equipped with SCIENCETECH FRSS AM 1.5 G filter giving 1 sun conditions. The amount of H_2 gas generation, from the effluent of the reaction mixture, was measured every 15 min, using an on-line micro-Gas chromatography unit (Agilent Technologies 3000) having a molecular sieve column (MolSieve 5 A) equipped with a Thermal Conductivity Detector (TCD). The H_2 generation tests were repeated three times using fresh sample at the same conditions to obtain the average H_2 generation with error bars. The apparent

quantum efficiency (AQE) of the photocatalytic materials are calculated using equation (1) below [22], and detailed calculations are shown in the supplementary information (S1).

$$AQE = \frac{Number\ of\ reacted\ electrons}{Toatal\ umber\ of\ photons\ absorbed} \times 100 \qquad (1)$$

The stability of the optimized samples TiO_2-CdS (3:2) was tested in a photocatalytic H_2 generation test for 40 consecutive hours (hr) at the same conditions as described for regular H_2 generation tests.

3. Results and discussion

3.1 Morphological analysis

The morphology of the pure CdS nanoparticles and a representative core-shell TiO_2-CdS nanocomposite sample (TiO_2-CdS (3:2)) is analyzed by using the field emission scanning electron microscopy (FE-SEM), as shown in Fig. 1. Pure CdS nanoparticles, having conical shapes, with size ~70 nm show clear grain boundaries in Fig. 1a. It can be seen from the image in Fig. 1b that the TiO_2 is thoroughly covering the agglomerated CdS nanoparticles, forming a core-shell structure. Fig. 1c and 1d illustrate the dark field images of pure CdS and the TiO_2-CdS (3:2) sample, respectively. The clear and uniform surface of the CdS nanoparticles at high magnification is observed in Fig. 1c. TiO_2 covering the CdS nanoparticles forming the core-shell structure is demonstrated by the difference in contrast of CdS nanoparticles with TiO_2 in Fig. 1d. Furthermore, to confirm the core-shell structure of TiO_2-CdS, energy dispersive X-ray spectroscopy (EDX) elemental mapping was also performed for the optimized sample. The overall EDX elemental mapping Fig. 1 (e) and separate EDX elemental maps (Fig S2) reveals the presence of Cd, S, Ti and O in TiO_2-CdS (3:2) sample, and shows that Ti and O are

distributed over a larger area than Cd and S, confirming the formation of the core-shell structure in the TiO_2-CdS (3:2) sample.

3.2 Crystalline structure

X-ray diffraction (XRD) patterns of pure CdS nanoparticles, pure TiO_2 and various samples of core-shell TiO_2-CdS nanocomposite are shown in Fig. 2. XRD diffraction patterns of pure CdS and pure TiO_2 exhibit characteristic peaks associated with the pure wurtzite structure of CdS which match well with JCPDS card no. 80-0006 [17,23] and accordingly the anatase phase of TiO_2 in agreement with JCPDS card no. 83-2243 [24]. XRD patterns of core-shell TiO_2-CdS nanocomposites show the presence of the wurtzite form of CdS and the anatase phase of TiO_2 in all the samples. As the amount of TiO_2 content increases in the TiO_2-CdS samples, the intensity of the diffraction peaks (101), (004) and (204) increases, while the rest of the diffractions peaks are being overlapped by the diffraction peaks of CdS and hence not visible.

3.3 N_2-physisorption analysis

The shape of all N_2 sorption isotherms for all samples is revealing a type IV isotherms according to the IUPAC classification [25] as shown in Fig. S3. The isotherms show H3 hysteresis loop indicating the presence of slit-like pores with plate-like particles [25]. Pure CdS and pure TiO_2 exhibits Brunaner-Emmett-Teller (BET) surface areas of 21 $m^2\ g^{-1}$ and 1475 $m^2\ g^{-1}$, respectively. As the nanocomposite samples are formed, the surface area increases sharply and reaches a maximum value of 110 $m^2\ g^{-1}$ for the optimized sample, *i.e.* TiO_2-CdS (3:2). By further increasing the content of TiO_2 on CdS, the surface area remains unchanged in TiO_2-CdS (4:2) sample as shown in Table S1. The BJH pore size distribution of all samples is shown in Fig. S4 and average pore width values are tabulated in Table S1 in showing that all samples

have pore sizes in the range, 2-50 nm, confirming the mesoporous nature of the TiO_2-CdS nanocomposite [26].

3.4 Optical properties

Pure CdS nanoparticles show an absorption onset at *ca.* 500 nm with a broad absorption in visible range which is due to the intrinsic band gap transition of an electron from the valence band to the conduction band [27] as shown in Fig. 3. Pure TiO_2 exhibited an absorption edge around 380 nm in the UV-vis spectrum, which is associated with the characteristic band gap transmission [28]. The UV-vis DRS spectra of the nanocomposite samples exhibited enhanced absorption in the visible and UV region in comparison to pure CdS and pure TiO_2. The band gap (E_g) of pure CdS nanoparticles and pure TiO_2 are shown in Fig S5 which is calculated by using the Tauc's relationship. Pure CdS and pure TiO_2 exhibited a band gap energy of 2.2 eV and 3.0 eV, which are close to the reported values of hexagonal CdS and anatase, respectively [29,30].

The photoluminescence (PL) spectra of pure CdS nanoparticles, pure TiO_2 and the optimized sample TiO_2-CdS (3:2) are shown in Fig. S6. The pure CdS and pure TiO_2 exhibit PL peaks around 563 nm and 380 nm, which are corresponding to the recombination of photo-induced electrons and holes in the conduction band and valence band of the respective material. The PL peak in the TiO_2-CdS (3:2) sample around 563 nm has disappeared. This indicates restricted recombination of photo-induced electrons and holes, therefore prolonged lifetime of the charge carrier due to the formation of the in-build heterojunction between CdS and TiO_2, which in turn gives the enhanced photocatalytic activity due to the increased photo-induced charge separation [31].

3.5 *Surface analysis*

To investigate the electronic state and oxidation state of the elements present in all the samples, XPS was performed. Fig. S7 shows the measured Ti 2p, O 1s, Cd 3d and S 2p spectra of the TiO_2-CdS (3:2) nanocomposite sample in addition to those of the pure TiO_2 and pure CdS. The Ti 2p core level (Fig. S7a) exhibits two spin-orbit split contributions with Ti $2p_{3/2}$ and Ti $2p_{1/2}$ components located around 458.5 eV and 464.2 eV respectively, confirming the presence of Ti (IV) in the pure TiO_2 and TiO_2-CdS (3:2) samples [32,33]. Cd in pure CdS and TiO_2-CdS (3:2) is in the +2 oxidation state as judged by the Cd $3d_{5/2}$ and Cd $3d_{3/2}$ contributions located at binding energies of 404.9 eV and 411.7 eV, respectively (Fig. S7b). This is in agreement with the values reported in literature [32,34]. The S 2p spectra in Fig. S7c includes two spin-orbit split peaks with binding energies of 161.4 eV and 162.5 eV corresponding to S $2p_{3/2}$ and S $2p_{1/2}$, respectively. This confirms that S is in the −2 valence state for the pure CdS and TiO_2-CdS (3:2) samples [35,36]. The intensity of Cd and S peaks in TiO_2-CdS (3:2) is lower than the pure CdS samples, which indicates that the CdS nanoparticles are covered by TiO_2 with thickness less than 10 nm [37]. The slight shift in the binding energy with respect to peak position of Cd and S relative to the pure CdS sample may be due to the interaction of CdS and TiO_2 on the interface of the heterojunction [38]. The O 1s spectra shown in Fig. S7d, consists mainly of Ti-O bonded oxygen with binding energy around 529.7 eV for pure TiO_2 and TiO_2-CdS (3:2). A minor O 1s component present at the high binding energy side (~531.1 eV) is ascribed to hydroxyl groups and/or defects present in the surface region [33,39].

3.6 *Photocatalytic H_2 generation tests*

Fig. 4 shows the cumulative photocatalytic H_2 generation by different samples as a function of time in the presence of 0.125 M Na_2S and 0.175 M Na_2SO_3 acting as hole scavengers. Pure

CdS nanoparticles yield 686.4 μmol g^{-1} h^{-1} of hydrogen during the photocatalytic reaction while pure TiO_2 generates 565.5 μmol g^{-1} h^{-1} on average. In the nanocomposite samples, as the amount of TiO_2 increases in the core-shell structure of TiO_2-CdS nanocomposites, the photocatalytic hydrogen generation rate increases and after reaching the maximum value, it again decreases. The best performance is shown by the TiO_2-CdS (3:2) sample, which is producing 954 μmol g^{-1} h-^{1} of hydrogen, approximately 1.4 times better than pure CdS nanoparticles and about 1.7 times higher than pure TiO_2. Further increase of TiO_2 loading on CdS leads to a lower photocatalytic activity for the TiO_2-CdS (4:2) sample, which is due to less absorption of light in the visible region as shown in the UV-vis DRS results. The apparent quantum efficiency (AQE) of all the synthesized samples is shown in Table S1, and the most active sample exhibits enhanced AQE of 3.53% which is relatively high compared to reported values presented in Table S2.

The stability of the most active sample, *i.e.* TiO_2-CdS (3:2) is tested by performing the H_2 generation reaction in the same setup for 40 consecutive hr. The sample exhibits a constant rate of hydrogen generation over a period of 40 hr (as shown in Fig. S8) showing that the sample TiO_2-CdS (3:2) is a stable and active photocatalyst for hydrogen generation from water.

3.7 Photocatalytic H_2 generation mechanism

It is well established that the photocatalytic activity of the photocatalysts is showing a positive dependency with the BET surface area and the porosity of the material as also observed in our system [44]. As the shell thickness of the TiO_2 increases on the surface of CdS nanoparticles, the surface areas, as well as the photocatalytic activity of the samples increase exponentially achieving the maximum value represented by the optimized sample, *i.e.* TiO_2-CdS (3:2) as shown in Fig. S9. With further increase in the TiO_2 content of the TiO_2-CdS samples, no

increase in surface area is observed with the decrease in photocatalytic activity. Furthermore, The UV-vis DRS results confirm that the light absorption of the TiO_2-CdS (4:2) sample is also lower in comparison to TiO_2-CdS (3:2) sample due to the increase in the thickness of the TiO_2 shell on the CdS core. The PL measurements confirm that efficient charge separation is taking place on the interface of CdS and TiO_2 due to the formation of the in-built heterojunction.

To understand the underlying H_2 generation mechanism from water splitting by the CdS-TiO_2 samples, the theoretical valence band potential and conduction band potential of pure CdS and pure TiO_2 are calculated by employing the following empirical formulas (2) and (3) [40]:

$$E_{valence} = X - E + 1/2\ E_g \qquad (2)$$

$$E_{conduction} = E_{valence} - E_g \qquad (3)$$

Where, E_g represents the bandgap which is measured by employing Tauc plot relationship using the UV-vis spectra. $E_{valence}$ and $E_{conduction}$ represent valence band potential and conduction band potential, respectively. E represents the energy of a free electron on the hydrogen scale having a value of 4.5 eV. The value of X represents the electronegativity of the semiconductor material, which is calculated by taking the geometric mean of the electronegativity values of all the constituents [41,42]. The calculated values of $E_{valence}$, $E_{conduction}$, X, E_g for pure CdS and TiO_2 are tabulated in Table S3. The $E_{valence}$ and $E_{conduction}$ values of CdS are estimated at 1.38 eV and -0.82 eV, and those for TiO_2 are at 2.82 eV and -0.20 eV respectively, which are in good accordance with the reported values [43].

The combination of experimental and calculated values reveal that the conduction band potential of CdS has a more negative value than that of TiO_2. Upon photo-irradiation, CdS will first have photo-induced electron charge separation due to a lower band gap. The photo-induced electron generated in the conduction band of CdS is transferred to the conduction band of TiO_2 resulting in an increase of total electrons in the conduction band of TiO_2 [38,45]. The

electron from the conduction band of TiO_2 then takes part in the redox reaction of H^+ ions from water to generate H_2 since the redox potential for H^+/H_2 is less negative than the conduction band of TiO_2. Similarly, the holes from the valence band of TiO_2 migrates toward the valence band of CdS which have a more positive potential. The total number of holes from the valence band of CdS are neutralized by the electrons donated by the hole scavenger by electron tunneling effects [46]. The schematic diagram of the proposed reaction mechanism is shown in Fig. 5. In conclusion, the photocatalytic activity is enhanced by the combined effect of an increase in surface area of the TiO_2-CdS (3:2), enhanced solar spectrum absorption and efficient charge separation of light-induced charge carriers.

4. Conclusions

Aiming towards the development of cost-effective, solar light active and highly stable photocatalysts, core-shell TiO_2-CdS nanocomposite photocatalysts were synthesized by a facile two-step hydrothermal approach. The shell thickness of TiO_2 on CdS nanoparticles was optimized by varying the amount of TiO_2 precursor during synthesis in order to obtain enhanced photocatalytic activity for H_2 generation from water splitting using a solar simulator. The TiO_2-CdS (3:2) sample showed enhanced photocatalytic activity compared to pure CdS and pure TiO_2 along with promising stability. The enhanced photocatalytic activity is mainly attributed to broader light absorption, efficient photo-induced charge separation and high surface area due to the formation of a heterojunction between CdS and the high surface area TiO_2. The high stability of the photocatalyst is caused by the formation of the TiO_2 shell on the CdS nanoparticles, shielding the CdS particles from photo-corrosion by efficient hole neutralization during the photocatalytic reaction. The core-shell approach for stabilizing the

inherently unstable CdS material is effective for achieving enhanced photocatalytic activity and stability.

Acknowledgments

The authors acknowledge The Research Council of Norway through support of the NTNU NanoLab (grant number 245963) for providing the material characterization tools. The authors would also like to thank NTNU for financial support.

References

[1] S.E. Hosseini, M.A. Wahid, Energy Rev. 57 (2016) 850–866.

[2] J. a. Herron, J. Kim, A. a. Upadhye, G.W. Huber, C.T. Maravelias, Energy Environ. Sci. 8 (2015) 126–157.

[3] T. Gao, Z. Chen, Q. Huang, F. Niu, X. Huang, L. Qin, Y. Huang, Rev. Adv. Mater. Sci. 40 (2015) 97–109.

[4] W. Wang, M.O. Tadé, Z. Shao, Chem. Soc. Rev. 44 (2015) 5371–5408.

[5] Z.-F. Huang, L. Pan, J.-J. Zou, X. Zhang, L. Wang, Nanoscale. 6 (2014) 14044–14063.

[6] O.C. Compton, F.E. Osterloh, J. Phys. Chem. C. 113 (2009) 479–485.

[7] M. Mishra, D.-M. Chun, Appl. Catal. A Gen. 498 (2015) 126–141.

[8] P. Dhanasekaran, H.G. Salunke, N.M. Gupta, J. Phys. Chem. C. 116 (2012) 12156–12164.

[9] K. Maeda, Phys. Chem. Chem. Phys. 15 (2013) 10537.

[10] S. Cao, J. Yu, J. Photochem. Photobiol. C Photochem. Rev. 27 (2016) 72–99.

[11] Y. Zhang, L. Han, C. Wang, W. Wang, T. Ling, J. Yang, C. Dong, F. Lin, X.-W. Du, ACS Catal. 7 (2017) 1470–1477.

[12] V.M. Daskalaki, M. Antoniadou, G. Li Puma, D.I. Kondarides, P. Lianos, Environ. Sci. Technol. 44 (2010) 7200–7205.

[13] Z.-R. Tang, B. Han, C. Han, Y.-J. Xu, J. Mater. Chem. A. 5 (2017) 2387–2410.

[14] Z. Lian, P. Xu, W. Wang, D. Zhang, S. Xiao, X. Li, G. Li, ACS Appl. Mater. Interfaces. 7 (2015) 4533–4540.

[15] Y. Wei, J. Jiao, Z. Zhao, W. Zhong, J. Li, J. Liu, G. Jiang, A. Duan, J. Mater. Chem. A. 3 (2015) 11074–11085.

[16] S. Qian, C. Wang, W. Liu, Y. Zhu, W. Yao, X. Lu, J. Mater. Chem. 21 (2011) 4945.

[17] H.H. El-Maghrabi, A. Barhoum, A.A. Nada, Y.M. Moustafa, S.M. Seliman, A.M. Youssef, M. Bechelany, J. Photochem. Photobiol. A Chem. 351 (2018) 261–270.

[18] J. Jang, H. Gyukim, P. Borse, J. Lee, Int. J. Hydrogen Energy. 32 (2007) 4786–4791.

[19] Y.J. Zhang, W. Yan, Y.P. Wu, Z.H. Wang, Mater. Lett. 62 (2008) 3846–3848.

[20] S. Han, Y.-C. Pu, L. Zheng, J.Z. Zhang, X. Fang, J. Mater. Chem. A. 3 (2015) 22627–22635.

[21] S. Han, L. Hu, N. Gao, A.A. Al-Ghamdi, X. Fang, Adv. Funct. Mater. 24 (2014) 3725–3733.

[22] X. Zhang, D. Luo, W. Zhang, W. Gao, X. Ning, H. Liu, B. Tian, B. Yang, G. Lu, Appl. Catal. B Environ. 232 (2018) 371–383.

[23] S.E. Haque, B. Ramdas, A. Sheela, N. Padmavathy, Nano Lett. 9 (2014) 731–735.

[24] J. Fang, L. Xu, Z. Zhang, Y. Yuan, S. Cao, Z. Wang, L. Yin, Y. Liao, C. Xue, ACS Appl. Mater. Interfaces. 5 (2013) 8088–8092.

[25] M. Kruk, M. Jaroniec, Chem. Mater. 13 (2001) 3169–3183.

[26] K.S.W. Sing, D.H. Everett, R.A.W. Haul, L. Moscou, R.A. Pierotti, J. Rouquerol, T. Siemieniewska, Pure Appl. Chem. 57 (1985) 603–619.

[27] Y. Wang, Y. Wang, R. Xu, J. Phys. Chem. C. 117 (2013) 783–790.

[28] M. Zubair, H. Kim, A. Razzaq, C.A. Grimes, S.-I. In, J. CO2 Util. 26 (2018) 70–79.

[29] Q. Xiang, B. Cheng, J. Yu, Appl. Catal. B Environ. 138–139 (2013) 299–303.

[30] A. Duta, M. Visa, S.A. Manolache, M. Nanu, in: 2008 11th Int. Conf. Optim. Electr. Electron. Equip., IEEE, 2008: pp. 461–466.

[31] S. Liu, N. Zhang, Z.-R. Tang, Y.-J. Xu, ACS Appl. Mater. Interfaces. 4 (2012) 6378–6385.

[32] L. Wu, J.C. Yu, X. Fu, J. Mol. Catal. A Chem. 244 (2006) 25–32.

[33] J. C. Yu, J. Yu, H. Y. Tang, L. Zhang , J. Mater. Chem. 12 (2002) 81–85.

[34] L. Ma, T. Zhang, R. Song, L. Guo, Int. J. Hydrogen Energy. (2018).

[35] N. Zhang, S. Liu, X. Fu, Y.-J. Xu, J. Mater. Chem. 22 (2012) 5042.

[36] M. Zubair, A. Razzaq, C.A. Grimes, S. Il In, J. CO2 Util. 20 (2017) 301–311.

[37] Z. Chen, Y.-J. Xu, ACS Appl. Mater. Interfaces. 5 (2013) 13353–13363.

[38] G. Li, L. Wu, F. Li, P. Xu, D. Zhang, H. Li, Nanoscale. 5 (2013) 2118.

[39] J.C. Yu, J. Yu, J. Zhao, Appl. Catal. B Environ. 36 (2002) 31–43.

[40] Y. Xu, M.A.A. Schoonen, Am. Mineral. 85 (2000) 543–556.

[41] D.C. Ghosh, T. Chakraborty, J. Mol. Struct. THEOCHEM. 906 (2009) 87–93.

[42] M.S. Oskoui, M. Khatamian, M. Haghighi, A. Yavari, RSC Adv. 4 (2014) 19569.

[43] C. Xue, T. Wang, G. Yang, B. Yang, S. Ding, J. Mater. Chem. A. 2 (2014) 7674–7679.

[44] S.-C. Jung, Korean J. Chem. Eng. 25 (2008) 364–367.

[45] Y. Lu, X. Cheng, G. Tian, H. Zhao, L. He, J. Hu, S.-M. Wu, Y. Dong, G.-G. Chang, S. Lenaerts, S. Siffert, G. Van Tendeloo, Z.-F. Li, L.-L. Xu, X.-Y. Yang, B.-L. Su, Nano Energy. 47 (2018) 8–17.

[46] D. Jiang, Z. Sun, H. Jia, D. Lu, P. Du, J. Mater. Chem. A. 4 (2016) 675–683.

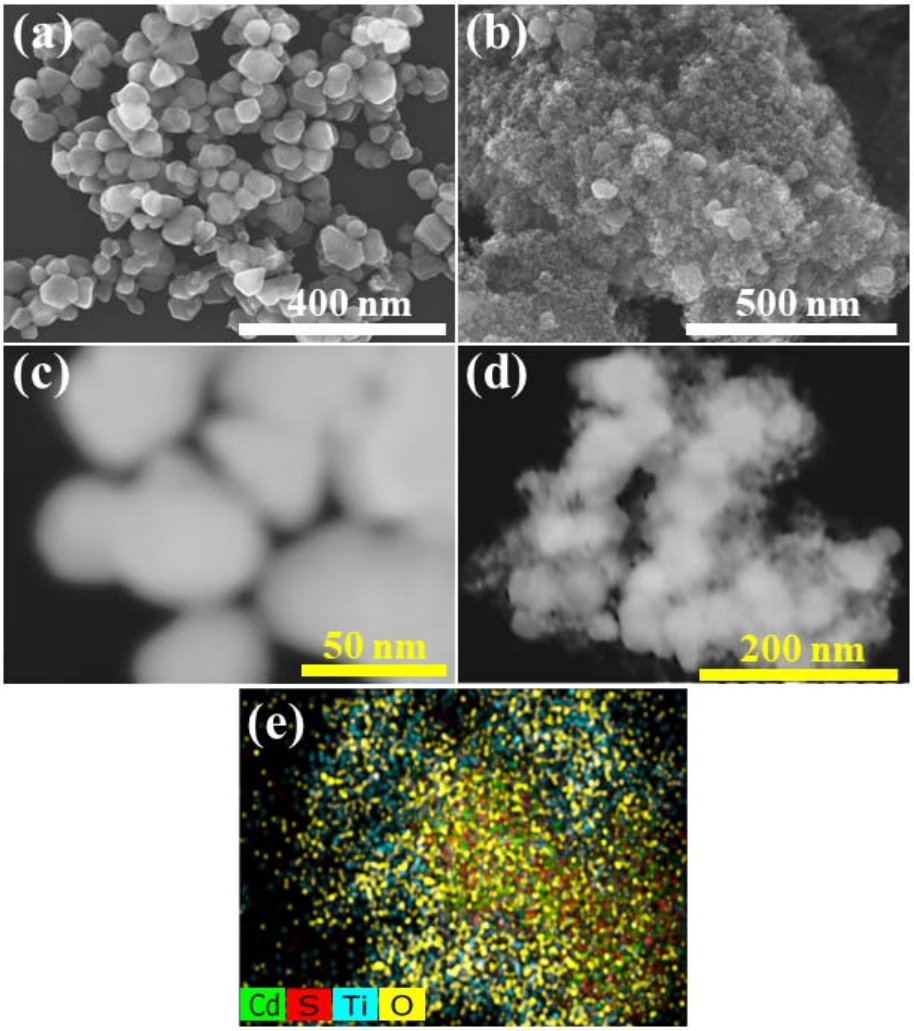

Fig. 1 FE-SEM images of (a) pure CdS nanoparticles, (b) TiO_2-CdS (3:2), (c) dark field SEM image of pure CdS nanoparticles (d) dark field SEM image of TiO_2-CdS (3:2) and (e) the overall EDX elemental mapping of TiO_2-CdS (3:2).

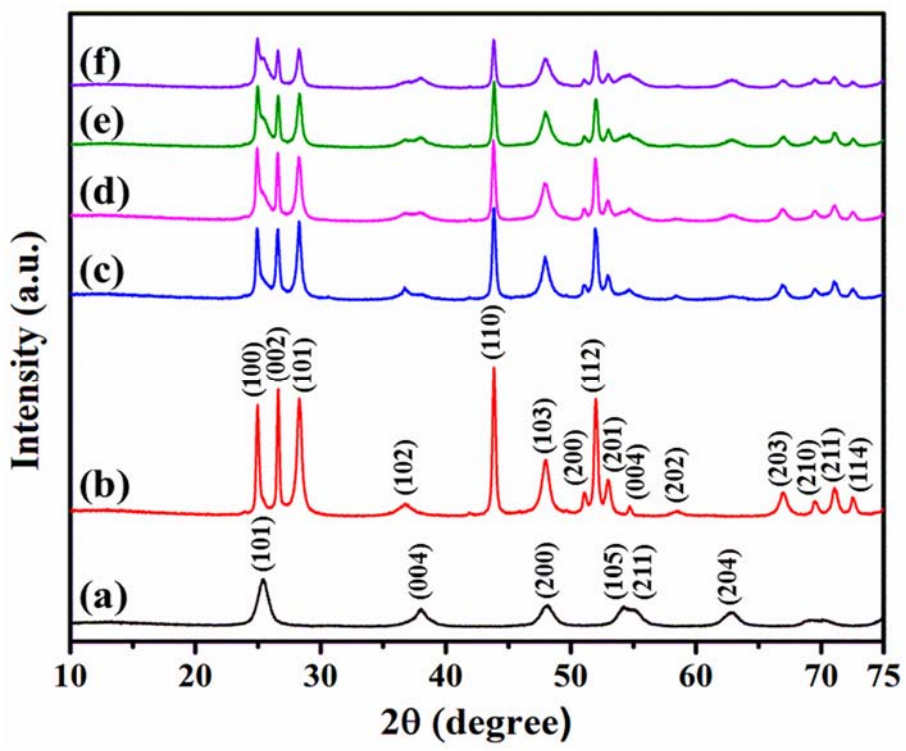

Fig. 2 XRD patterns of (a) pure TiO_2, (b) pure CdS nanoparticles, (c) TiO_2-CdS (1:2), (d) TiO_2-CdS (2:2) (e) TiO_2-CdS (3:2) and (f) TiO_2-CdS (4:2) samples.

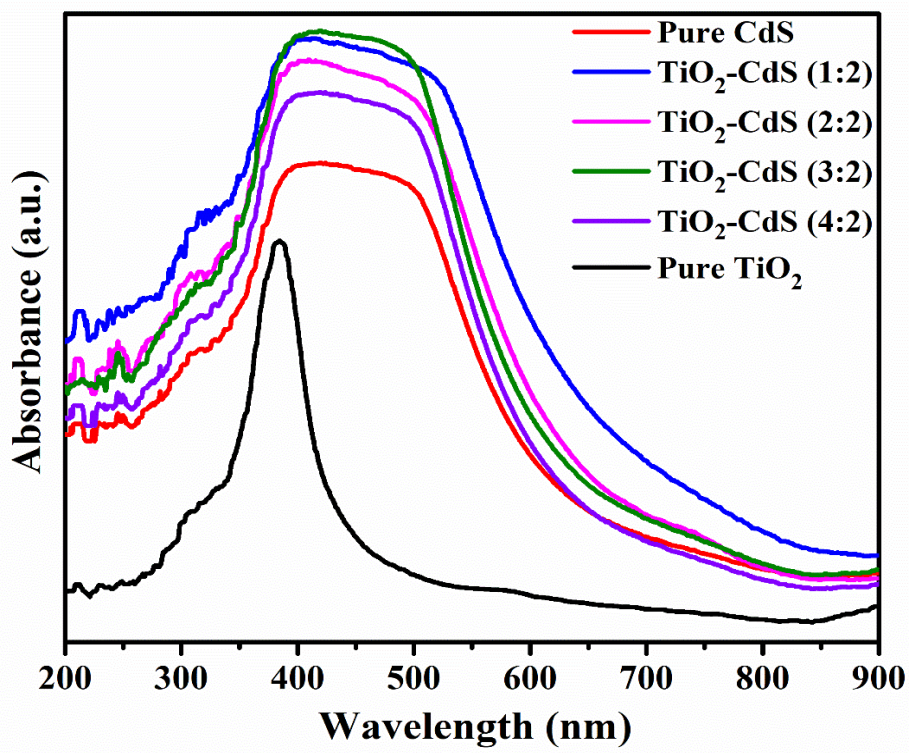

Fig. 3 UV-vis DRS spectra of pure TiO_2, pure CdS nanoparticles, TiO_2-CdS (1:2), TiO_2-CdS (2:2), TiO_2-CdS (3:2) and TiO_2-CdS (4:2) samples.

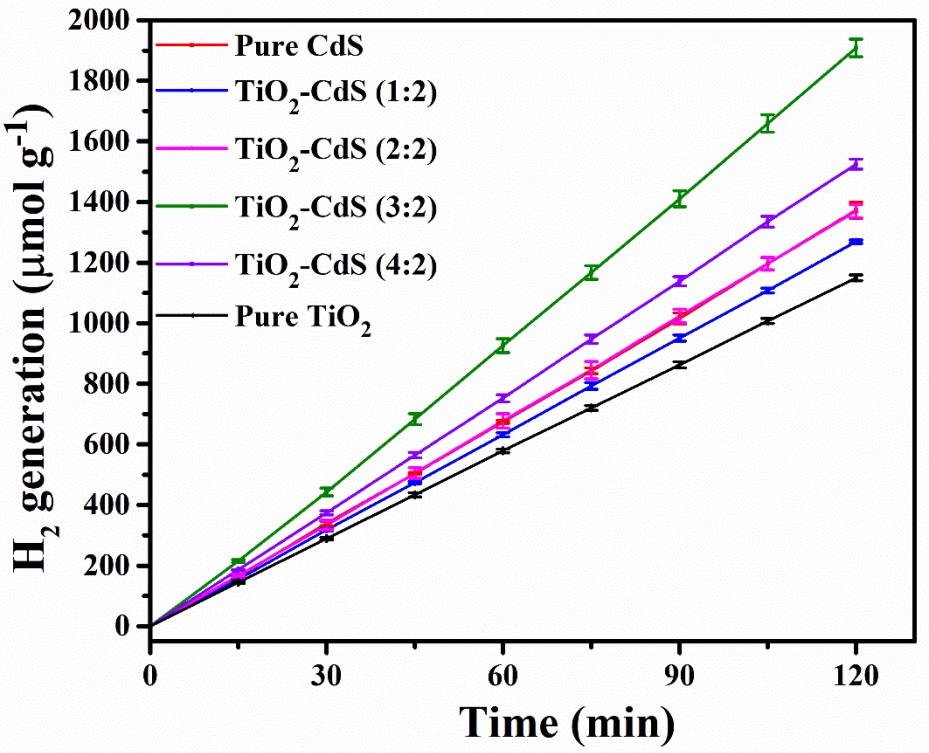

Fig.4 Photocatalytic H_2 generation rate by using pure CdS nanoparticles, pure TiO_2 and TiO_2-CdS samples under simulated solar light at AM 1.5G conditions.

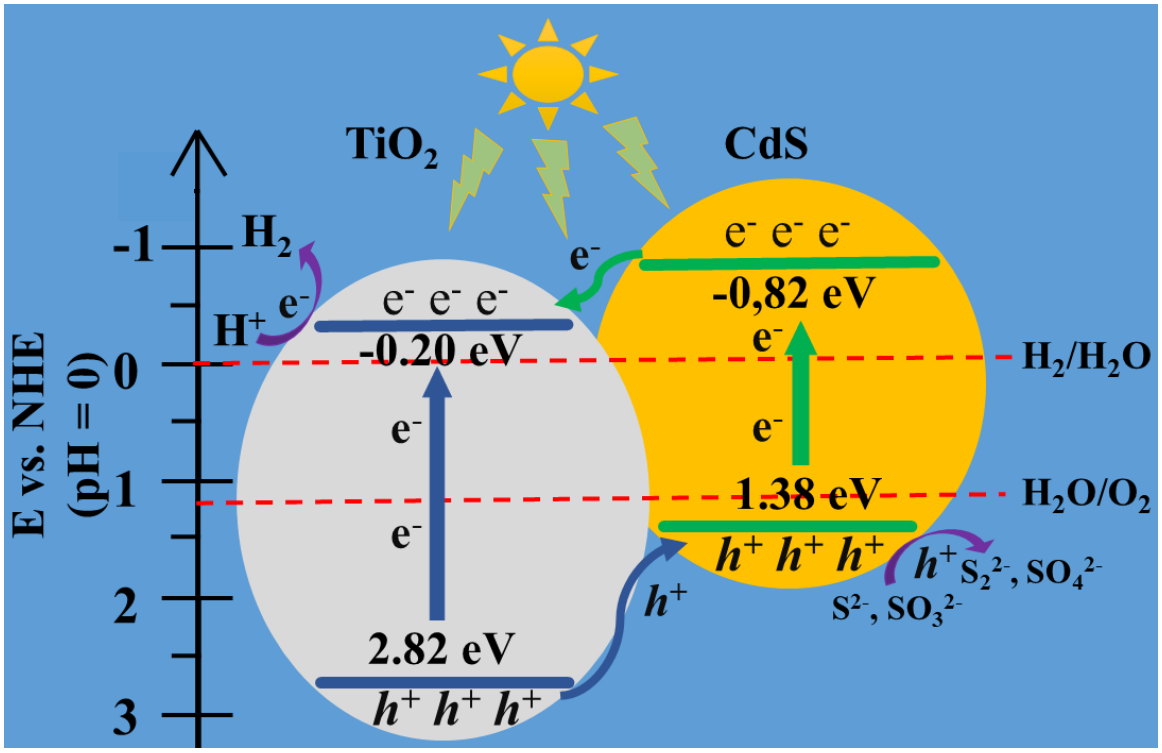

Fig. 5 Proposed reaction mechanism for photocatalytic H_2 generation from water over the CdS-TiO_2 nanocomposite catalysts.